Temporal Change in Seismic Wave Attenuation Using High-stable Vibration Sources.

Shuhei TSUJI (shuhei.tsuji@gmail.com)
Nagoya Daigaku Daigakuin Kankyogaku Kenkyuka

Koshun Yamaoka
Nagoya University Graduate School of Environmental Studies: Nagoya Daigaku Daigakuin Kankyogaku Kenkyuka

Ryoya Ikuta
Shizuoka Daigaku

Full paper

Keywords: attenuation, amplitude, coseismic change, anisotropy, artificial seismic source, ACROSS

Posted Date: March 11th, 2021

DOI: https://doi.org/10.21203/rs.3.rs-236736/v1

Title page:

Title: Temporal change in seismic wave attenuation using high-stable vibration sources.

Author #1: (Corresponding Author) Shuhei Tsuji, Graduate School of Environmental Studies, Nagoya University, Furo-cho, Chikusa-ku, Nagoya 464-8601, Japan, stsuji@seis.nagoya-u.ac.jp

Author #2: Koshun Yamaoka, Earthquake and Volcano Research Center, Graduate School of Environmental Studies, Nagoya University, Furo-cho, Chikusa-ku, Nagoya 464-8601, Japan, kyamaoka@seis.nagoya-u.ac.jp

Author #3: Ryoya Ikuta, Faculty of Science, Shizuoka University, 836 Oya, Suruga, Shizuoka 422-8529, Japan, ikuta.ryoya@shizuoka.ac.jp

(go to new page)

Abstract

We developed a method to detect attenuation changes during seismic wave propagation excited by precisely controlled artificial seismic sources, namely Accurately Controlled Routinely Operated Signal System (ACROSS), and applied it to monitor the temporal changes for in situ data collected by previous studies. Our method, together with the use of the ACROSS sources, is less susceptible to noise level changes, from which conventional methods such as envelope calculation suffer. The method utilizes the noise level that is independently estimated in the frequency domain and eliminates the influence of the noise from the observed signal. For performance testing, we applied this method to a dataset that was obtained in an experiment at Awaji Island, Japan, from 2000 to 2001. We detected a change in amplitude caused by rainfall, variation in atmospheric temperature, and coseismic ground motions. Among them, coseismic changes are of particular interest because there are limited studies on coseismic attenuation change, in contrast to many studies on coseismic velocity decrease. At the 2000 Western Tottori earthquake (M_W = 6.6, epicenter distance of 165 km), a sudden decrease in amplitude of up to 5% was observed. The coseismic amplitude reduction and its anisotropic

characteristics, which showed a larger reduction in the direction of the major axis of velocity decrease, were consistent with the opening of fluid-filled cracks, as proposed by previous studies. The ΔQ^{-1} corresponding to the amplitude change gives similar values to those reported in previous studies using natural earthquakes.

Keywords

attenuation; amplitude; coseismic change; anisotropy; artificial seismic source;

ACROSS

Main Text

Introduction

Temporal changes in the propagation property of seismic waves have been studied using both seismic velocity and attenuation. In previous studies, coseismic changes, among others, have drawn the attention of researchers because they display clear synchronization to earthquakes and their relation to relevant phenomena can be discussed quantitatively. A decrease in seismic velocity is often reported as a typical phenomenon

46 in earthquakes. Various methods have been used to detect seismic velocity changes at
47 earthquakes in many locations. Seismic interferometry (Brenguier et al. 2008; Hobiger et
48 al. 2016; Ikeda and Tsuji 2018), which does not require artificial sources, is generally
49 used to measure the temporal variation in seismic velocity in recent years. In contrast,
50 experiments with artificial seismic sources (Ikuta et al. 2002; Yang et al. 2014; Tsuji et al.
51 2018) were conducted to identify coseismic velocity changes with better resolution. In
52 most cases the seismic velocity decreases during the earthquakes and recovers gradually
53 over time. These phenomena are accounted for by the fracturing of subsurface rock
54 (Sawazaki et al. 2009; Nakata and Snieder 2011) and/or crack opening by stress (Grêt et
55 al. 2006; Silver et al. 2007) or pore pressure changes (Ikuta and Yamaoka 2004; Sawazaki
56 and Snieder 2013) caused by the strong ground motions of earthquakes.
57 Fracturing, crack opening, and saturation increase of pore fluid cause attenuation,
58 as shown in laboratory experiments (Lockner et al. 1977; Toksöz et al. 1979; Tao and
59 King 1990; Best et al. 2007; Chichinina et al. 2009; Amalokwu et al. 2014; Zaima and
60 Katayama 2018). These studies measured the changes in attenuation with fluid saturation
61 and confining pressure, and reported an increase in attenuation with crack opening and

62 saturation. Attenuation with cracks is interpreted as an increase in friction loss on the
63 crack surface and/or energy loss due to fracture to generate cracks. The attenuation with
64 saturation is interpreted as an increase in viscous losses in the cracks and/or with fluid
65 flowing through the microchannels between cracks.

66 Coseismic changes in attenuation were also detected in the field. The spectral
67 ratio of natural earthquakes (Chun et al. 2004; Titzschkau et al. 2010; Kelly et al. 2013)
68 and coda-Q (Sato 1986; Fehler et al. 1988; Huang and Kisslinger 1992; Domínguez R. et
69 al. 2003; Sugaya et al. 2009; Padhy et al. 2013) have been used. They are used to estimate
70 the temporal variation in attenuation in the region surrounding earthquake faults or in
71 volcanic regions. The analysis based on the spectral ratio assumed a model in which Q is
72 independent of frequency, for example, because the amplitudes of the sources are difficult
73 to estimate precisely. However, when we use artificial sources, the assumption may not
74 be necessary. Yamamura et al. (2003) used a piezo-electric actuator, which produces
75 seismic signals of a constant amplitude, as a seismic source to reveal the periodic
76 variation in attenuation associated with earth tides. Despite the use of seismic sources
77 with high resolution, no remarkable earthquakes occurred during their experiment, and

78 they did not detect a coseismic change of attenuation.

79 We developed effective methods for high stability artificial sources to
80 measure the temporal change in amplitude of seismic signals. We used the Accurately
81 Controlled Routinely Operated Signal System (ACROSS) as a highly stable artificial
82 source, which makes it possible to obtain accurate transfer functions. The stability of the
83 ACROSS source is a principal advantage of measuring the temporal variation in
84 attenuation, which is difficult to acquire when using natural seismic sources. The
85 ACROSS was developed for precise monitoring of propagation properties through
86 continuous seismic waves excited by a precisely controlled rotating eccentric weight
87 (Kumazawa and Takei 1994), which enables us to continuously obtain precise transfer
88 functions between sources and receivers (Kumazawa et al. 2007). With these
89 characteristics, ACROSS is able to monitor small variations in the medium in various
90 fields, such as the Sakurajima Volcano, Japan (Yamaoka et al. 2014; Maeda et al. 2015),
91 or the Nankai Trough subduction zone (Tsuji et al. 2018).

92 Another advantage of estimating amplitude variation using ACROSS is the
93 noise level estimation during the signal observation. Amplitude estimation of the signal

94 can be affected by temporal variations in background noise. For example, the signal
95 amplitude can be overestimated when we use the envelope of the signal in the time
96 domain. In the usual operations of the ACROSS source, the noise level and the signal
97 from the source are continuously monitored, which is achieved by a frequency
98 modulation (FM) of the source frequency at a precisely constant time interval. With this
99 operation, the signal has a discrete series in the frequency domain, and the background
100 noise appears between the signal peaks.

101 In this study, we demonstrate a method to estimate the temporal variation in
102 the amplitude by removing the noise variation effect, which is independently obtained
103 during the observation of the ACROSS source. Additionally, we demonstrate the
104 effectiveness of our method by applying it to the dataset obtained in a previous study by
105 Ikuta et al. (2002), in which coseismic change in the seismic velocity was clearly visible.
106 Ikuta et al. (2002) interpreted that the changes were caused by the self-opening of the
107 preferred oriented, fluid-filled cracks due to pore pressure increase. Their interpretation
108 is that the changes in seismic attenuation can be caused by viscous losses of fluid in the
109 cracks.

Method

Estimation of noise level

Our method fully utilized the unique characteristics of the signal generated by the ACROSS source. In general, ACROSS sources are operated with FM at a precise time period in repeating intervals. Thus, signal peaks of ACROSS appear with an interval of the reciprocal of the FM period in the frequency domain. In this operation, we can obtain spectral components that include only noise between all the signal components of ACROSS when Fourier transformation is applied to the data whose length is an integer multiple of the FM period. For example, when an identical modulation repeats every 10 s and Fourier transformation is applied on 50 s long data, the sampling interval in the frequency domain is 1/50 Hz, and the signal of the ACROSS source appears at every five samples (Figure 1). We refer to the spectral components including the ACROSS signal as the “signal channel,” and other components that include only background noise as the “noise channel.”

As the background noise is also included in the signal channels of the ACROSS,

127 the noise causes a bias result in the estimation of the ACROSS signal amplitude.
128 Therefore, it is necessary to make an adequate estimation of the noise that overlaps the
129 signal, especially to estimate the temporal variation in the signal amplitude because the
130 level of the background noise varies with time. The noise in a signal channel can be
131 estimated from the neighboring noise channels under the assumption that the noise in
132 both channels have the same stochastic nature.

133 **Method to estimate the amplitude variation**

134 We estimated a temporal change in the amplitudes of a target phase (e.g., P or
135 S wave). The signal and noise variance for the target phases were estimated based on
136 the method of Ikuta et al. (2002). In their study, the transfer function in the frequency
137 domain G_k corresponding to the target phase was calculated as the following
138 convolution:

139 $$G_k = \sum_{j=0}^{N} \frac{X_j}{S_j} H_{k-j} \quad (1)$$

140 where X_j and S_j are the spectral components of the signal channel and the source
141 signal, respectively, H_{k-j} is the Fourier transform of the Hanning window, and N is
142 the number of signal channels used in the analysis. Similarly, we can calculate the noise

variance corresponding to G_k as

$$\sigma_k^2 = \sum_{j=0}^{N} \frac{\varepsilon_j^2}{S_j S_j^*} H_{k-j}^2 \quad (2)$$

where ε_j^2 is the variance of the noise in the signal channel, and calculated from the neighboring noise channels as

$$\varepsilon_j^2 = \frac{1}{M} \sum_{m=1}^{M} X_m X_m^* \quad (3)$$

where X_m is the spectral component of the noise channels neighboring the corresponding signal channel, * denotes the complex conjugate, and M is the number of noise channels used.

We express the temporal variations of the amplitude based on the total power ratio of the ACROSS signal at each time to those of reference transfer function. As the signal channel includes both signal and noise, the power of the signal can be estimated by subtracting the noise power from the power of the signal channel. Therefore, the ratio r can be calculated using the following equation:

$$r^2 = \frac{\sum_k (G_k G_k^* - \sigma_k^2)}{\sum_k G_{k0} G_{k0}^*} \quad (4)$$

where G_{k0} is the reference transfer function obtained using Equation (1). Summation

158 over all available components of the ACROSS signal are calculated.

159 The uncertainty of the ratio is given by

160 $$\sigma_{r^2} = \frac{\sqrt{\sum_k \left\{2G_k G_k^* \sigma_k^2 + 2\left(G_k^2 + {G_k^2}^*\right)(\alpha^2 - \beta^2) + \eta_k^2\right\}}}{\sum_k G_{k0} G_{k0}^*} \quad (5)$$

161 where α^2 and β^2 are the variances of the real and imaginary parts of the noise,

162 respectively, and η_k denotes the estimation error of σ_k^2. See the Appendix for the

163 derivation of Equation (5).

164

165 **Performance test with a synthetic data**

166 To demonstrate the advantage of our method, we conducted a performance test

167 with a synthetic dataset of signal and noise. By using the synthetic data, we estimated the

168 amplitude of the signal using our method and compared the result with that of the

169 envelope calculation. The signal was created as a series of spectral peaks with constant

170 amplitudes and random phases in a certain frequency range. The signal was converted to

171 a time series with inverse Fourier transform, and the synthetic data were obtained by

172 applying a Hanning window.

173 We produced frequency series with an increment of 0.01Hz, and inserted

174 spectral peaks between 10 and 20 Hz with a 0.1 Hz interval. It means 9 noise channels
175 between every neighboring pair of signal channels. A Hanning window between 2 s and
176 4 s was applied on the time series. Noises that follow a normal distribution with zero
177 mean were added to the time series.

178 We compared the amplitudes of the signal in the synthetic data estimated by
179 our method to that of the envelope calculation. Standard deviations of the noise were
180 given with a step of 0.01 from 0 to 5, which were normalized by the root mean square
181 (RMS) of the signal. We computed 1000 times for each step to compare the theoretical
182 estimation of error with the scattering of the data.

183 The results of the performance test are shown in Figure 2. The amplitudes
184 estimated with our method did not show systematic bias resulting from the noise. The
185 estimated amplitude average was almost constant with variable noise amplitudes. The
186 scattering of the amplitude estimation coincides with the theoretical error estimation. In
187 contrast, the estimation with the envelope calculation clearly has a bias result that
188 increases with noise amplitude.

189

190 **Application to the Awaji data**

191 The dataset used in this study was obtained in an experiment at the Awaji site
192 in western Japan (Ikuta et al. 2002; Ikuta and Yamaoka 2004), where a surface fault
193 appeared at the 1995 Hyogo-ken Nanbu (Kobe) Earthquake (M_{jma} = 7.3) (Nakata and
194 Yomogida 1995). At this site, an experiment with two ACROSS vibrators was conducted
195 for 15 months from January 2000 to April 2001. They monitored changes in travel time
196 for P and S waves and found coseismic delays in two earthquakes that caused relatively
197 large ground motion at the site (Ikuta et al. 2002; Ikuta and Yamaoka 2004).

198 The two ACROSS vibrators generated elastic waves with FM in different
199 frequency ranges covering between 10 to 23 Hz. As the FM period was 5 s, the sources
200 produced discrete signals with an interval of 0.2 Hz in the frequency domain. Unlike
201 recent experiments with ACROSS sources, no rotation switching had been implemented
202 at that time, that is, the weight rotated only clockwise from the top throughout the
203 experiment. Seismic waves excited by the ACROSS vibrators were recorded at the
204 bottoms of the two boreholes in the experiment site. The seismometers in the boreholes
205 are three-component velocity-type sensors with a natural frequency of 3 Hz and 2 Hz
206 for vertical and horizontal components in the 800 m deep borehole, and 4.5 Hz for the

207 1700 m deep borehole. Both sensors were located nearly vertically downward from the
208 sources with small horizontal distances of 50 m and 120 m from the vibrators (Figure
209 3).

210 We estimated a temporal change in attenuation using a series of transfer
211 functions that were obtained in Ikuta et al. (2002). In this study, we performed an
212 independent data screening to remove the observation period in which ACROSS
213 vibrators are not in proper operation. The first step of the data screening was conducted
214 based on the operation logs of the ACROSS source. The rotation frequency and mass
215 position were logged in at 1 s intervals and were used to eliminate the operation stop
216 period. The cross covariance of the transfer functions for each 1 h interval with the
217 reference time is also used for data screening in the second step. We removed the data
218 for which the cross covariances were less than 0.75. The low cross covariance may imply
219 flaws in the seismic observation systems.

220 After screening, the continuous wave records were divided into 100 s
221 segments that were stacked together in hourly intervals. Stacking was performed with a
222 weighted average adopting the inverse maximum amplitude in each segment as the

223 weight. The stacked waveforms were deconvolved with the source function of the
224 ACROSS vibrators' force in the frequency domain to obtain transfer functions. As we
225 used 100 s long data for stacking, its Fourier transform contained spectral components
226 with an interval of 0.01 Hz. As the period of FM was 5 s, the source signal provided
227 spectral components with an interval of 0.2 Hz. This caused the ACROSS signal channel
228 to appear with every 20 components in the frequency series for each vibration source.
229 We selected P and S waves in the transfer function in the time domain, which
230 is calculated by the inverse Fourier transformation of the signal channel. P and S waves
231 were selected for the 800 m and 1700 m boreholes in the same way as Ikuta et al. (2002)
232 and Ikuta and Yamaoka (2004) for comparison. The waveforms that included either P or
233 S waves were selected with a 20% Hanning window of 0.3 s centered at the travel time
234 of P or S waves estimated from the typical velocity of the country rock. P waves were
235 selected from the vertical components, and S waves were selected from the horizontal
236 components (Figure 4). The transfer functions in the time domain, shown in Figure 4,
237 were obtained by inverse Fourier transformation of those in the frequency domain. P, S,
238 and several later phases were identified in the transfer functions for the seismometers in

239 both the 800 m and 1700 m boreholes.

240 We applied our method to P and S waves. For S waves, we analyzed the signal
241 of each component of the seismometers instead of synthetizing the radial and transverse
242 components. Thus, we name two horizontal components, H1 and H2, for both sensors in
243 the 800 m and 1700 m boreholes. The H1 and H2 components in the 800 m borehole were
244 directed N126°E and N216°E, and those of the 1700 m borehole were directed N90°E
245 and N180°E. The S phase that appears in each component is denoted as S-H1 and S-H2.

246 The estimation errors of the amplitude variation were calculated based on
247 Equation (5). The dataset of the experiments obtained by Ikuta et al. (2002) only includes
248 the mean amplitude of the noise channels for each of the signal channels. Thus, we
249 assume that the variances of the real and imaginary parts of the noise (α^2 and β^2 in
250 Equation 5) are identical, and η_k^2 is negligible. We calculated the estimation error of
251 the amplitude variation using the following equation:

252 $$\sigma_{r^2} = \frac{\sqrt{\sum_k 2G_k G_k^* \sigma_k^2}}{\sum_k G_{k0} G_{k0}^*} \quad (6)$$

253

Results

Temporal changes in travel time and amplitude

Temporal variations in the amplitudes and travel times estimated for P, S-H1, and S-H2 observed by the sensors in the 800 m and 1700 m boreholes are shown in Figure 5. The hourly data shows the daily and long-term, or event-related, variations. This study calculated the variation in travel time for each component and illustrated the hourly variation instead of the plots in Ikuta et al. (2002), which showed radial and transverse components with a moving average over 24 h.

We confirmed that the variations in travel time are similar to those in Ikuta et al. (2002) (see the top three panels in Figure 5). Long-term variation in P and S waves, such as gradual delay from January to March and gradual advance from April to May in 2000, were observed. A sudden delay in extremely heavy rain on September 11 was observed in all the components. The delay was preceded by a two-month-long advance of travel time, which corresponds to the dry summer season at this site. This change has been interpreted by Ikuta et al. (2002)as the change in the source motion with reference to the weight rotation caused by the change in energy dissipation immediately local to the source. Coseismic delay and gradual recovery were observed at the teleseismic event on

October 6, 2000. In addition, changes that may be associated with the second and fourth water injection experiments were observed for the 800 m borehole, although Ikuta et al. (2002) did not mention this event.

Several characteristics of the amplitude variation were seen in the experimental period (see the bottom three panels in Figure 5). The overall pattern of the amplitude variation in P waves was similar for both the 800 m and 1700 m boreholes and gradually decreased from January to February, soon after the onset of the ACROSS experiment. The extremely heavy rainfall on September 11 also changed the amplitudes of the S wave after a gradual change from mid-August. The amplitude of S-H1 decreases for the 800 m borehole after a gradual increase but increases for the 1700 m borehole after a gradual decrease. However, only a few changes were observed in P and S-H2. In contrast to the travel time change, it is difficult to interpret the cause of the amplitude variation with only the source-ground interaction. A possible cause is the interference of multipath waves that suffer radiation variation near the source.

Diurnal variations that correlated well with temperature changes (Figure 6) were observed. For the 800 m borehole, the amplitude had a positive correlation with

287 temperature for all the phases. The P and S-H1 showed a larger variation than that of S-
288 H2. The maximum variation in P and S-H1 reached approximately 5%, while S-H2
289 reached approximately 3%. For the 1700 m borehole, P and S-H1 showed a positive
290 correlation with the temperature, whereas S-H2 showed a negative correlation. The daily
291 variation in P (approximately 10%) is larger than that of S-H1 and S-H2 (approximately
292 3%).

293 On October 31, 2000, a step-like decrease in the amplitude of all the phases
294 for the 1700 m boreholes was observed. This coincides with the time when the top of the
295 borehole was opened for temperature measurement (Yamano and Goto 2005).
296 Interestingly, no change was observed in the travel time. This may be caused by a change
297 in the coupling between the sensors and the surrounding rock, which may reduce only the
298 amplitude. The change in the coupling of the sensor might be caused by the change in the
299 water flow in the borehole induced by the opening of the well top.

300

301 **Coseismic Change**

302 During the ACROSS experiment, four earthquakes with relatively large
303 ground motions were observed at the site. Among them, two earthquakes, the Western

304 Tottori Earthquake (WT) on October 6, 2000, and the Geiyo Earthquake (GY) on
305 February 8, 2001, showed coseismic change in amplitude as well as seismic velocity. The
306 magnitudes and epicenter distances of WT and GY were 6.6 and 165 km, and 6.4 and 215
307 km, respectively.

308 Figure 6 shows the temporal changes in amplitude during the ten days before
309 and after the earthquakes. The amplitude decreases for both earthquakes, and the change
310 at the WT was greater than that at the GY, which followed the same tendency as travel
311 times. For the WT, a sudden drop of approximately 3% and 5% were observed in S-H2
312 for the 800 m borehole and S-H1 for the 1700 m borehole, respectively. Gradual
313 recoveries lasted approximately one week after the earthquakes were observed in P and
314 S for both boreholes (Figure 6a). The amplitude recovered to a similar level as before the
315 earthquake. In contrast, for the GY, only S-H2 of the 800 m borehole showed a clear step-
316 like decrease of 1% (Figure 6b). Gradual recoveries were barely observed in any of the
317 phases of the sensor.

318

319 **Change at water injections**

320 In this experiment site, water injection experiments were conducted

321 repeatedly from 1997 to monitor healing process in the Nojima Fault zone after the
322 1995 Kobe Earthquake (Ando 2001). Four injection operations were conducted during
323 the ACROSS operation period. The first operation was performed on January 4, 2000 but
324 was aborted due to the leakage of water at the well top. The second, third, and fourth
325 operations were successfully performed on January 22–26, January 31 to February 5, and
326 March 3–11, respectively. During these three operations, the water was injected at
327 constant pressures of 2.9, 4.0, and 4.5 MPa, respectively. A total of 457 kL of water was
328 injected during the four operations (Nishigami 2001). Water was pumped into the 1700
329 m borehole to feed the water into the bedrock. It is assumed that the water leaked to the
330 bedrock at a depth of 580 m, which was revealed by temperature monitoring using an
331 optical fiber thermometer (Yamano and Goto 2001).
332 Significant changes in the transfer function in both the amplitude and travel
333 time were observed during two of the four injection operations (Figure 7). Increases in
334 amplitude were observed in P and S-H1 of the 800 m borehole in the second and fourth
335 periods of water injection. The timing of the increases in travel times were similar to those
336 of the increase in amplitude. However, no significant change was observed in the third

337 period. The similarity of the variation between the amplitude and travel time with the
338 variation in the atmospheric temperature in the second and fourth periods indicates that
339 the changes during the periods of the water injection experiment may be due to changes
340 in atmospheric temperature. Variation in the atmospheric temperature might change the
341 elastic property of the surface part of the ground around the ACROSS source and affect
342 the transfer function.
343

344 # Discussions

345 **Anisotropy of the coseismic changes**

346 Anisotropic changes in travel time were a key aspect in revealing the
347 mechanism of coseismic change in Ikuta and Yamaoka (2004). In this chapter, we aim
348 to analyze the anisotropic nature of coseismic change in attenuation. We reinvestigated
349 anisotropic change in travel time and conducted a method to estimate anisotropy of the
350 amplitude change with the ACROSS monitoring data.

351 Ikuta and Yamaoka (2004) estimated the orientation of anisotropy by
352 calculating the coseismic change of S wave splitting. They calculated the magnitude of

353 the coseismic delay of S waves in six directions by rotating the oscillation direction with
354 an interval of 30 °. They estimated the direction of the principal axes of anisotropy by
355 fitting an ellipse to the azimuthal distribution of the delay. We reanalyzed the anisotropy
356 of coseismic changes in the same way, except for the azimuthal interval. We estimated
357 the travel time delays with an azimuthal interval of one degree using the following
358 procedure.

359 We used the transfer functions between 100 h before and 24 h after the
360 earthquakes and synthesized transfer functions for all directions. We calculated the
361 changes in travel time of the transfer functions using cross spectrum with reference to the
362 average of the transfer functions in the first 24 h of the selected period. Because large
363 variations that are quite similar to the changes in atmospheric temperature are observed,
364 we reduced the effect of the atmospheric temperature by assuming that the variation
365 follows a linear function of temperature. We calculated the coefficients of the linear
366 function using the data obtained from the 100 h before the earthquakes.

367 The coseismic delay in each direction is modeled by the following equation,

368 $$M(t) = at + \mathrm{H}(t - T) \cdot \{b(t - T) + c\} \quad (7)$$

where a represents the change rate before the earthquake, $\mathrm{H}(t)$ denotes the Heaviside step function, b represents the recovery rate after the earthquake, c is the coseismic step, t is the time from the beginning of the modeling period, and T is the time of the earthquake. We estimated the parameters a , b and, c with a least square method.

Figure 8 shows the azimuthal variation in the coseismic delay with a one degree interval. Our result coincides with the result of Ikuta and Yamaoka (2004) at their calculation azimuths. However, the azimuthal pattern of coseismic delay may not be approximated by an orbit as they did for fewer data points.

To reveal the meaning of the pattern, we performed a simulation with synthetic transfer functions. We modeled the wave that traveled vertically downward in a uniformly anisotropic media from the ACROSS source. As the S wave from the ACROSS source is expressed as two components of sinusoidal vibration with a right angle and a phase difference of $\pi/2$, we used the direction of the two components of the transfer function as the principal axes of anisotropy. The transfer function in the principal axes in the frequency domain can be written as

$$\begin{cases} S_1(\omega) = \exp\{i\phi(\omega)\} \\ S_2(\omega) = A\exp\left[i\left\{\phi(\omega) + \dfrac{\pi}{2} + \omega\delta t_0\right\}\right] \end{cases} \tag{8}$$

where ω is the angular frequency of the signal, $\phi(\omega)$ is the initial phase for each angular frequency, and δt_0 is the difference in travel time due to the anisotropy of the surrounding media. We assumed that the amplitude ratio between the two functions, A and ω, is constant and provided $\phi(\omega)$ as a uniformly distributed random number between 0 and 2π.

We assumed that the principal axes of anisotropy do not change, we got the transfer functions after the coseismic step as follows:

$$\begin{cases} \widetilde{S_1} = \exp[i\{\phi(\omega)\} + \omega\delta t_1] \\ \widetilde{S_2} = A\exp\left[i\left\{\phi(\omega) + \frac{\pi}{2} + \omega(\delta t_0 + \delta t_2)\right\}\right] \end{cases} \tag{9}$$

where δt_1 and δt_2 are the steps in travel time in the directions of S_1 and S_2. Next, we synthesized a transfer function with a linear combination for the direction angle θ as follows:

$$S_\theta = S_1\cos\theta + S_2\sin\theta \tag{10}$$

$$\widetilde{S_\theta} = \widetilde{S_1}\cos\theta + \widetilde{S_2}\sin\theta \tag{10a}$$

We calculated the delay in travel time as a function of θ and found the azimuthal patterns similar to those shown in Figure 8. We can reproduce a similar pattern by giving proper parameters in the calculation, as shown in Figure 9.

401 By using this model, we updated the azimuthal direction of the principal axes
402 of anisotropy. We searched for the parameters that provide the best fit to the observed
403 angular pattern shown in Figure 8 using the least squares method. The parameters we
404 searched for were δt_0, δt_1, δt_2, A, and azimuthal direction of the major axis of
405 anisotropy. The major axis denotes the principal axis showing larger delay. As the
406 calculation has a trade-off between δt_0 and A, A is given independently with the
407 observed transfer function. A is given as the ratio of the amplitude of the transfer
408 functions in the azimuthal direction of two principal axes of anisotropy.
409 The results are shown in Figure 10. For WT, the directions of the major axis
410 were N90°E for both the 800 m and 1700 m borehole sensors. For GY, the directions
411 were N85°E and N95°E for the 800 m and 1700 m borehole sensors, respectively. These
412 directions coincide well with the results of Ikuta and Yamaoka (2004), in which the
413 direction was N100°E for WT and GY at the 800 m sensors.
414 Now, we can estimate the anisotropic change in amplitude using the directions
415 of the principal axes of velocity anisotropy. In our simulation, we found that the azimuthal
416 variation in the amplitude was affected by the change in the travel time even if no change

417 in amplitude was given to the synthetic data. However, the changes in amplitude are not
418 affected by the travel time change for the direction of the principal axes, which is apparent
419 from Equations (8)–(10). Therefore, the anisotropy of coseismic change in amplitude is
420 evaluated using the variation in the direction of the principal axes of anisotropy.

421 Changes in the amplitude and result of the model fitting are shown in
422 Figure 11. The coseismic change in the two principal axes are estimated using the same
423 procedure as for the travel time analysis. We also corrected the daily variation correlated
424 with the atmospheric temperature. For WT, a greater decrease in amplitude is obtained in
425 the major axis of velocity anisotropy for both depths. For GY, no significant difference
426 was observed for either depths.

427 Our results show that the direction of greater attenuation corresponds to that
428 of larger delay, which are consistent with laboratory experiments with cracked and
429 saturated media (Tao and King 1990; Chichinina et al. 2009). Thus, the attenuation
430 anisotropy is consistent with the mechanism of coseismic change proposed by Ikuta and
431 Yamaoka (2004).

Rotation invariant value of change in amplitude

The result of our simulation indicates that the estimation of amplitude change based on a single component may give artificial results, especially for S waves. As indicated by Equations (10) and (10a), the sum of the square of the two components with a right angle gives a solution that is independent of the azimuthal angle θ. Therefore, we may use the RMS of two horizontal components of transfer functions as azimuth invariant values. An equation to obtain the invariant amplitude for the S wave can be derived from Equation (4) as follows:

$$\widetilde{r^2} = \frac{\sum_k \{(G_{1_k} G_{1_k}^* + G_{2_k} G_{2_k}^*) - (\sigma_{1_k}^2 + \sigma_{2_k}^2)\}}{\sum_k (G_{1_{k0}} G_{1_{k0}}^* + G_{2_{k0}} G_{2_{k0}}^*)} \tag{11}$$

where subscripts 1 and 2 indicate the components of H1 and H2, respectively, and $G_{1_{k0}}$ and $G_{2_{k0}}$ are the reference transfer functions. Figure 12 shows the change in the invariant amplitude for the entire period. As a result, we confirmed the coseismic changes at WT and GY, and some other changes associated with the heavy rain and opening of the well top.

Comparison of coseismic change in terms of Q

We tried to convert the changes in amplitude to that of Q^{-1} for comparison with

449 the coseismic changes observed in other studies. When we assumed that Q is independent

450 of frequency, the amplitude ratio γ can be written as

451 $$\gamma(f) = \frac{\frac{1}{d}A\exp\left(-\frac{2\pi f d}{2c}Q^{-1}\right)}{\frac{1}{d}A\exp\left(-\frac{2\pi f d}{2c}Q_0^{-1}\right)} = \exp\left(-\frac{\pi f d}{c}\Delta Q^{-1}\right) \quad (12)$$

452 where d is the distance of the sensors from the source, A is the amplitude at the source,

453 ω is the angular frequency of an elastic wave, c is the velocity of an elastic wave, and

454 Q_0^{-1} and Q^{-1} are the inverse of the quality factor before and after the earthquake,

455 respectively. We provided $\Delta Q^{-1} = Q^{-1} - Q_0^{-1}$.

456 We may assume that the amplitude ratio obtained in this study, before and after

457 the earthquake, is equivalent to the amplitude ratio γ at the mean frequency used in our

458 experiment $\bar{f}$. Then, the change in ΔQ^{-1} can be written as follows:

459 $$\Delta Q^{-1} = -\frac{c}{\pi \bar{f} d}\ln(\alpha) \quad (13)$$

460 where α is the ratio of the amplitudes before and after the earthquake in this study. The

461 amplitude ratio in this study is calculated by $(1 + aT + c)/(1 + aT)$ using a, T, and

462 c in Equation (7). Herein, we assumed no velocity change in the equation because the

463 coseismic velocity change was sufficiently small (< 0.5%).

464 We calculated ΔQ^{-1} for the P-UD component and the change in the invariant

amplitude of the S wave using Equation (13). We used $V_P = 4.0\ [km/s]$, $V_S = 2.5\ [km/s]$ for c, and 16 Hz for $\bar{f}$ as the typical velocity of the surrounding rocks and the center of the source frequency of the ACROSS operation. Table 1 shows the amplitude ratio, and Table 2 shows ΔQ^{-1} calculated by Equation (13).

Table 1: The amplitude ratio of coseismic step

	Step at WT		Step at GY	
	0800 m	1700 m	0800 m	1700 m
P	0.96	0.98	--	--
S	0.97	0.95	0.99	--

The amplitude ratio of the transfer functions before and after the earthquakes in each sensor and each phase. "--" indicates that no significant change was observed.

Table 2: ΔQ^{-1} corresponding to the amplitude ratio

	Step at WT		Step at GY	
	0800 m	1700 m	0800 m	1700 m
P	3.72×10^{-3}	2.00×10^{-3}	--	--
S	0.98×10^{-3}	1.53×10^{-3}	0.34×10^{-3}	--

ΔQ^{-1} estimated using Equation (13) with the amplitude ratio shown in Table 1, $V_P = 4.0\ [km/s]$, $V_S = 2.5\ [km/s]$, and $\bar{f} = 16$ Hz.

These ΔQ^{-1} values have a similar order of magnitude as reported in previous studies using spectral ratio methods. For example, Kelly et al. (2013) reported that ΔQ^{-1} in the fault region of the 2004 Parkfield Earthquake (MW = 6.0) was of the order of 1.0 $\times 10^{-3}$. Wang and Ma (2015) found a decrease in Q_S associated with the 1999 Chi-Chi Earthquake (M_W = 7.6). The Q_S was changed from 238 to 157, which corresponds to 2.2 $\times 10^{-3}$ of ΔQ^{-1}.

Conclusions

We developed a method to detect amplitude changes by utilizing the stable artificial seismic source, ACROSS, and applied it to in-situ data. The amplitude change was obtained by calculating the ratio of the power of the transfer function of each period to that of the reference time. The noise that is estimated independent of the signal is used to avoid an apparent change in amplitude caused by the drift of the noise level. We applied this method to the data acquired by Ikuta et al. (2002). A coseismic decrease in amplitude was detected for two earthquakes with a maximum decrease of approximately 5%. The anisotropy of the coseismic changes showed that the direction of larger delay in travel time shows a greater decrease in amplitude. This result is consistent with the results

494 of laboratory experiments with cracked media. We calculated ΔQ^{-1} of the coseismic
495 change corresponding to the amplitude change, and consistent values with previous
496 studies were obtained.
497
498
499 # Declarations
500 **Availability of data and materials**
501 Please contact Dr. Ikuta Ryoya for the transfer functions and operation
502 logs that we used for this analysis.
503 Precipitation and temperature data at Gunka station were retrieved from
504 the JMA website (http://www.data.jma.go.jp/gmd/risk/obsdl/index.php ,
505 In Japanese).
506 **Competing interests**
507 The authors declare that they have no competing interests.
508 **Funding**
509 This study was founded by Nagoya University.

Authors' contributions

TS developed the method, carried out the analysis, and drafted the manuscript. YK supervised the TS and developed the method together. IR provided the data of the experiments at Awaji Site and supported the development of the method. All authors have read and approved the final manuscript.

Acknowledgements

We used meteorological data from an AMeDAS station managed by JMA. We used GMT5 (Wessel et al. 2013) to draw maps. We would like to thank Editage (www.editage.com) for English language editing.

References

Amalokwu K, Best AI, Sothcott J, Chapman M, Minshull T, Li XY (2014) Water saturation effects on elastic wave attenuation in Porous rocks with aligned fractures. Geophys J Int 197:943–947 . https://doi.org/10.1093/gji/ggu076

Ando M (2001) Geological and geophysical studies of the Nojima Fault from drilling:

526 An outline of the Nojima Fault zone probe. Isl Arc 10:206–214 .
527 https://doi.org/10.1111/j.1440-1738.2001.00349.x
528 Best AI, Sothcott J, McCann C (2007) A laboratory study of seismic velocity and
529 attenuation anisotropy in near-surface sedimentary rocks. Geophys Prospect
530 55:609–625 . https://doi.org/10.1111/j.1365-2478.2007.00642.x
531 Brenguier F, Campillo M, Hadziioannou C, Shapiro NM, Nadeau RM, Larose E (2008)
532 Postseismic relaxation along the San Andreas Fault at Parkfield from continuous
533 seismological observations. Science (80) 321:1478–1481 .
534 https://doi.org/10.1126/science.1160943
535 Chichinina TI, Obolentseva IR, Ronquillo-Jarillo G (2009) Anisotropy of seismic
536 attenuation in fractured media: Theory and ultrasonic experiment. Transp Porous
537 Media 79:1–14 . https://doi.org/10.1007/s11242-008-9233-9
538 Chun K-Y, Henderson GA, Liu J (2004) Temporal changes in P wave attenuation in
539 the Loma Prieta rupture zone . J Geophys Res Solid Earth 109:1–15 .
540 https://doi.org/10.1029/2003jb002498
541 Domínguez R. T, Flores C. F, Reyes D. G (2003) Temporal change in coda wave

attenuation observed at Volcán de Colima, México before the 1998 eruption. J Volcanol Geotherm Res 125:215–223 . https://doi.org/10.1016/S0377-0273(03)00096-9

Fehler M, Roberts P, Fairbanks T (1988) A temporal change in coda wave attenuation observed during an eruption of Mount St. Helens. J Geophys Res Solid Earth 93:4367–4373 . https://doi.org/10.1029/JB093iB05p04367

Grêt A, Snieder R, Özbay UU (2006) Monitoring in situ stress changes in a mining environment with coda wave interferometry. Geophys J Int 167:504–508 . https://doi.org/10.1111/j.1365-246X.2006.03097.x

Hobiger M, Wegler U, Shiomi K, Nakahara H (2016) Coseismic and post-seismic velocity changes detected by passive image interferometry: Comparison of one great and five strong earthquakes in Japan. Geophys J Int 205:1053–1073 . https://doi.org/10.1093/gji/ggw066

Huang ZX, Kisslinger C (1992) Coda-Q before and after the 1986 Andreanof Islands earthquake. Pure Appl Geophys PAGEOPH 138:1–16 . https://doi.org/10.1007/BF00876711

Ikeda T, Tsuji T (2018) Temporal change in seismic velocity associated with an offshore MW 5.9 Off-Mie earthquake in the Nankai subduction zone from ambient noise cross-correlation. Prog Earth Planet Sci 5:62 . https://doi.org/10.1186/s40645-018-0211-8

Ikuta R, Yamaoka K (2004) Temporal variation in the shear wave anisotropy detected using the Accurately Controlled Routinely Operated Signal System (ACROSS). J Geophys Res Solid Earth 109:B09305 . https://doi.org/10.1029/2003JB002901

Ikuta R, Yamaoka K, Miyakawa K, Takahiro K, Mineo K (2002) Continuous monitoring of propagation velocity of seismic wave using ACROSS. Geophys Res Lett 29:1627 . https://doi.org/10.1029/2001GL013974

Kelly CM, Rietbrock A, Faulkner DR, Nadeau RM (2013) Temporal changes in attenuation associated with the 2004 M6.0 Parkfield earthquake. J Geophys Res Solid Earth 118:630–645 . https://doi.org/10.1002/jgrb.50088

Kumazawa M, Kunitomo T, Nakajima T, Tsuruga K, Hasada Y, Nagao H, Matsumoto H, Kasahara J, Fujii N, Shigeta N (2007) Development of ACROSS (Accurately Controlled, Routinely Operated, Signal System) to realize constant monitoring the

574 invisible Earth's interiors by means of stationary coherent elastic and
575 electromagnetic waves. Tokai Mura, Naka-gun, Ibaraki-ken, Japan (In Japanese
576 with English abstract)
577 Kumazawa M, Takei Y (1994) Active method of monitoring underground structures by
578 means of Accurately Controlled ROtary Seismic Source (ACROSS). 1. Purpose
579 and principle. Abstruct Seismol. Soc. Japan p158 (In Japanese)
580 Lockner DA, Walsh JB, Byerlee JD (1977) Changes in seismic velocity and attenuation
581 during deformation of granite. J Geophys Res 82:5374–5378 .
582 https://doi.org/10.1029/JB082i033p05374
583 Maeda Y, Yamaoka K, Miyamachi H, Watanabe T, Kunitomo T, Ikuta R, Yakiwara H,
584 Iguchi M (2015) A subsurface structure change associated with the eruptive
585 activity at Sakurajima Volcano, Japan, inferred from an accurately controlled
586 source. Geophys Res Lett 42:5179–5186 . https://doi.org/10.1002/2015GL064351
587 Nakata N, Snieder R (2011) Near-surface weakening in Japan after the 2011 Tohoku-
588 Oki earthquake. Geophys Res Lett 38:1–5 . https://doi.org/10.1029/2011GL048800
589 Nakata T, Yomogida K (1995) Surface Fault Characteristics of the 1995 Hyogoken-

590 Nambu Earthquake. J Nat disaster Sci 16:1–9

591 Nishigami K (2001) Summary of the wather injection experiment, shallow structure of

592 the Nojima fault and its healing process. Chikyu Mon 23:232–235 (In Japanese)

593 Padhy S, Takemura S, Takemoto T, Maeda T, Furumura T (2013) Spatial and temporal

594 variations in coda attenuation associated with the 2011 Off the Pacific Coast of

595 Tohoku, Japan (Mw 9) earthquake. Bull Seismol Soc Am 103:1411–1428 .

596 https://doi.org/10.1785/0120120026

597 Sato H (1986) Temporal change in attenuation intensity before and after the Eastern

598 Yamanashi Earthquake of 1983 in central Japan. J Geophys Res 91:2049 .

599 https://doi.org/10.1029/JB091iB02p02049

600 Sawazaki K, Sato H, Nakahara H, Nishimura T (2009) Time-lapse changes of seismic

601 velocity in the shallow ground caused by strong ground motion shock of the 2000

602 Western-Tottori earthquake, Japan, as revealed from coda deconvolution analysis.

603 Bull Seismol Soc Am 99:352–366 . https://doi.org/10.1785/0120080058

604 Sawazaki K, Snieder R (2013) Time-lapse changes of P- and S-wave velocities and

605 shear wave splitting in the first year after the 2011 tohoku earthquake, Japan:

606 Shallow subsurface. Geophys J Int 193:238–251 .
607 https://doi.org/10.1093/gji/ggs080
608 Silver PG, Daley TM, Niu F, Majer EL (2007) Active Source Monitoring of Cross-Well
609 Seismic Travel Time for Stress-Induced Changes. Bull Seismol Soc Am 97:281–
610 293 . https://doi.org/10.1785/0120060120
611 Sugaya K, Hiramatsu Y, Furumoto M, Katao H (2009) Coseismic change and recovery
612 of scattering environment in the crust after the 1995 Hyogo-ken Nanbu earthquake,
613 Japan. Bull Seismol Soc Am 99:435–440 . https://doi.org/10.1785/0120080012
614 Tao G, King MS (1990) Shear-wave velocity and Q anisotropy in rocks: A laboratory
615 study. Int J Rock Mech Min Sci 27:353–361 . https://doi.org/10.1016/0148-
616 9062(90)92710-V
617 Titzschkau T, Savage M, Hurst T (2010) Changes in attenuation related to eruptions of
618 Mt. Ruapehu Volcano, New Zealand. J Volcanol Geotherm Res 190:168–178 .
619 https://doi.org/10.1016/j.jvolgeores.2009.07.012
620 Toksöz MN, Johnston DH, Timur A, Toksöz MN, Timur A (1979) Attenuation of
621 seismic waves in dry and saturated rocks: I. Laboratory measurements.

GEOPHYSICS 44:681–690 . https://doi.org/10.1190/1.1440969

Tsuji S, Yamaoka K, Ikuta R, Kunitomo T, Watanabe T, Yoshida Y, Katsumata A (2018) Secular and coseismic changes in S-wave velocity detected using ACROSS in the Tokai region. Earth, Planets Sp 70:146 . https://doi.org/10.1186/s40623-018-0917-2

Wang Y-J, Ma K-F (2015) Investigation of the Temporal Change in Attenuation Within the Ruptured Fault Zone of the 1999 Mw7.3 Chi-Chi, Taiwan Earthquake. Pure Appl Geophys 172:1291–1304 . https://doi.org/10.1007/s00024-014-0854-3

Wessel P, Smith WHF, Scharroo R, Luis J, Wobbe F (2013) Generic mapping tools: Improved version released. Eos (Washington DC) 94:409–410 . https://doi.org/10.1002/2013EO450001

Yamamura K, Sano O, Utada H, Takei Y, Nakao S, Fukao Y (2003) Long-term observation of in situ seismic velocity and attenuation. J Geophys Res Solid Earth 108:1–15 . https://doi.org/10.1029/2002JB002005

Yamano M, Goto S (2005) Long-term monitoring of the temperature profile in a deep borehole: Temperature variations associated with water injection experiments and

638 natural groundwater discharge. Phys Earth Planet Inter 152:326–334 .
639 https://doi.org/10.1016/j.pepi.2005.04.010
640 Yamano M, Goto S (2001) Long-term temperature monitoring in a borehole drilled into
641 the Nojima Fault, Southwest Japan. Isl Arc 10:326–335 .
642 https://doi.org/10.1111/j.1440-1738.2001.00331.x
643 Yamaoka K, Miyamachi H, Watanabe T, Kunitomo T, Michishita T, Ikuta R, Iguchi M
644 (2014) Active monitoring at an active volcano: amplitude-distance dependence of
645 ACROSS at Sakurajima Volcano, Japan. Earth, Planets Sp 66:32 .
646 https://doi.org/10.1186/1880-5981-66-32
647 Yang W, Ge H, Wang B, Hu J, Yuan S, Qiao S (2014) Active source monitoring at the
648 Wenchuan fault zone: coseismic velocity change associated with aftershock event
649 and its implication. Earthq Sci 27:599–606 . https://doi.org/10.1007/s11589-014-
650 0101-0
651 Zaima K, Katayama I (2018) Evolution of Elastic Wave Velocities and Amplitudes
652 During Triaxial Deformation of Aji Granite Under Dry and Water-Saturated
653 Conditions. J Geophys Res Solid Earth 123:9601–9614 .

https://doi.org/10.1029/2018JB016377

Figure Captions

- Figure 1

Characteristics of the ACROSS signal in frequency domain

Typical distributions of the signal channels and noise channels in the frequency domain are illustrated. The signal channels appear at a constant interval, and noise channels appear in between. The intervals for the signal and noise channels are reciprocal of the modulation period and the data length, respectively.

- Figure 2

Result of the performance test

Amplitudes estimated using our method and the envelope calculation are shown by the dots in the left and right panels, respectively. Horizontal axes indicate the amplitude of noise relative to the root mean square of the signal. Vertical axes indicate the amplitude estimated with each method. The bold line shows the average of the calculation for each noise amplitude. The gray dashed line in the left panel indicates 95% confidence intervals, which are theoretically estimated from the noise

671 amplitude.

672 • Figure 3

673 Location of ACROSS vibrators and borehole seismometers

674 (a) Location of the site where ACROSS was deployed (yellow star) and epicenter of

675 two earthquakes, which are mentioned in the text (red stars). The area of the map (a)

676 is indicated by a black square in map (b). (c) Location of the ACROSS vibrator and

677 borehole seismometers on a vertical cross section. The yellow star indicates the

678 ACROSS vibrator. The red and blue circles show the 800 m and 1700 m sensors,

679 respectively.

680 • Figure 4

681 Reference transfer function in the time domain and selected P and S phases for the

682 800 m and 1700 m sensors.

683 Transfer functions on 14:00 January 19, 2000, are used as references. The area with

684 the red area shows the P and S phases selected for calculating the change in amplitude

685 and travel time. We selected P waves from the UD components (P-UD) and S waves

686 from two horizontal components (S-H1 and S-H2).

687 ● Figure 5

688 Change in travel time and amplitude throughout the observation period.

689 The changes in travel time (top three panels with yellow background) are calculated

690 according to Ikuta et al. (2002) and changes in amplitude (bottom three panels with

691 green background) are obtained by our method. The two panels in the middle

692 illustrate atmospheric temperature and rainfall observed at Gunka station, which is

693 the nearest meteorological station of the Japan Meteorological Agency. Blue

694 shading shows the periods of the water injection experiments. The red vertical lines

695 show the time of the earthquakes mentioned in the text. The gap between horizontal

696 lines with a pair of triangles in the left shows the mean error of the amplitude change

697 calculated by Equation (6). The colors of the lines and triangles correspond to

698 sensors in the legend on the right.

699 ● Figure 6

700 Changes in amplitudes 10 days before and after the 2000 Western Tottori (WT) and

701 2001 Geiyo (GY) earthquakes.

702 The bottom row shows the temperature and rainfall at Gunka station. The gap

between horizontal lines with a pair of triangles on the left of the panels shows the average error of the amplitude change.

- Figure 7

Change in amplitude during the period around the water injection experiments. The bottom row shows the temperature observed at the Gunka station. The blue background indicates the periods of the injection experiments. During the water injection experiment, the transfer function of the 1700 m sensor could not be analyzed because of the noise caused by the injection. The gap between horizontal lines with a pair of triangles on the right side of the panels show the mean error of the amplitude change.

- Figure 8

Azimuthal variation in the coseismic delay in travel time

The red line shows the azimuthal variation in the coseismic delay. The vertical and horizontal axes indicate the NS and EW directions, respectively. Distances from the origin indicate coseismic delay. Gray dashed lines indicate 95% confidence intervals. The top and bottom panels show the results for the 800 m and 1700 m sensors. The

719 left and right panels show the results for the WT and GY earthquakes, respectively.

720 • Figure 9

721 Examples of the synthetic azimuthal pattern

722 Azimuthal variations of delays calculated by synthetic dataset are shown as examples.

723 We showed three examples with 10, 5, and 0 ms of δt_0 in Equation (8). We provide

724 $A = 1, \delta t_1 = 1\ [ms], \delta t_2 = 2\ [ms]$ in Equations (8) and (9) for this calculation.

725 • Figure 10

726 Principal axes of the coseismic delay estimated with the parameter estimation

727 The red line shows the observed pattern. The orange line shows the synthetic pattern

728 with the best parameter. Solid and dashed green lines show the major and minor axes

729 of the principal axes, respectively. The top and bottom panels show the results for the

730 800 m and 1700 m sensors. The left and right panels show the results for the WT and

731 GY earthquakes, respectively.

732 • Figure 11

733 Coseismic decrease in amplitude in the principal axes of anisotropy

734 Major and minor axes denote the direction of principal axes with larger and smaller

735 delays in travel time, respectively. Variation in the amplitude (dots) and estimation
736 with our model (solid line) in the principal axes are shown. The top two rows show
737 the results for 800 m sensors and the bottom two rows show that for 1700 m sensors.
738 The left and right panels show the results for the WT and GY earthquakes,
739 respectively. The step and its estimation error are also shown on the left of each panel.
740 The red vertical line shows the time of the earthquake.

741 • Figure 12

742 Changes in amplitude of the azimuthal invariant value.

743 Changes in amplitude for P-UD and the azimuthal invariant value are shown in the
744 top and second panels. The atmospheric temperature and rainfall are shown in the
745 third and bottom panels. Periods with blue shading show the periods of the water
746 injection experiments. The red vertical lines show the time of the WT and GY
747 earthquakes.

748 Appendix 1: derivation of error formula

749 In the routine procedure of the analysis of ACROSS data, signal and noise
750 channels are separated in the frequency domain, as explained in the text. We may assume

751 that the noise in the signal channels has the same statistical property as the noise in the

752 noise channels. Therefore, a signal channel is composed of signal and noise as

753 $$G = G_0 + \varepsilon \quad (A1)$$

754 where G_0 is the signal and ε is the noise. Note that G_0 and ε are complex numbers.

755 The noise ε follows the statistical property as

756 $$\langle \varepsilon \rangle = 0 \quad (A2)$$

757 $$\langle \varepsilon \varepsilon^* \rangle = \sigma_0^2 \quad (A3)$$

758 where $<>$ represents the expectation and "$*$" denotes complex conjugate.

759 σ_0^2 is the variance of noise.

760 Because the noise variance is estimated from the noise channels around the

761 signal channel, the variance of the noise in the signal channel has an error δ. Thus, we

762 express the noise variance as:

763 $$\sigma^2 = \sigma_0^2 + \delta \quad (A4)$$

764 $$\langle \sigma^2 \rangle = \sigma_0 \quad (A5)$$

765 The error of the variance δ follows the statistical property as:

766 $$\langle \delta \rangle = 0 \quad (A6)$$

767 $$\langle \delta^2 \rangle = \eta^2 \quad (A7)$$

768 We calculate the expectation and variance of a component of the numerator of

769 Equation (4), which is the square of the signal subtracted by the variance of noise. The

770 expectation is expressed as follows:

771 $$\langle GG^* - \sigma^2 \rangle = \langle (G_0 G_0^* + G_0 \varepsilon^* + G_0^* \varepsilon + \varepsilon \varepsilon^*) - (\sigma_0^2 + \delta) \rangle$$

772 $$= G_0 G_0^* \quad (A8)$$

773 and the variance is expressed as

774 $$\langle (GG^* - \sigma^2 - G_0 G_0^*)(GG^* - \sigma^2 - G_0 G_0^*)^* \rangle$$

775 $$= \langle (G_0 \varepsilon^* + G_0^* \varepsilon + \varepsilon \varepsilon^* - \sigma_0^2 - \delta)(G_0 \varepsilon^* + G_0^* \varepsilon + \varepsilon \varepsilon^* - \sigma_0^2 - \delta)^* \rangle$$

776 $$= \langle 2 G_0 G_0^* \varepsilon \varepsilon^* + G_0^2 \varepsilon^{*2} + G_0^{*2} \varepsilon^2 + \varepsilon^2 \varepsilon^{*2} - 2 \varepsilon \varepsilon^* \sigma_0^2 - \sigma_0^4 - 2 \varepsilon \varepsilon^* \delta + 2 \sigma_0^2 \delta + \delta^2 \rangle$$

777 $$= 2 G_0 G_0^* \sigma_0^2 + G_0^2 \langle \varepsilon^{*2} \rangle + G_0^{*2} \langle \varepsilon^2 \rangle + \eta^2$$

778 $$= 2 G_0 G_0^* \sigma_0^2 + \left(G_0^2 + G_0^{*2} \right) (\alpha^2 - \beta^2)$$

779 $$+ \eta^2 \quad (A9)$$

780 where α^2 and β^2 denote the variance of the real and imaginary parts of ε,

781 respectively.

782 Because Equation (4) gives the amplitude by calculating the sum of the signal

783 channels, the error of the changes in the amplitude is expressed as

784 $$\sigma_{r^2} = \frac{\sqrt{\sum_k \{2G_{0_k} G^*_{0_k} \sigma^2_{0_k} + (G^2_{0_k} + G^{*2}_{0_k})(\alpha^2_k - \beta^2_k) + \eta^2_k\}}}{\sum_k G_{k0} G^*_{k0}} \quad (A10)$$

785 where k denotes the index of the signal channels. We may replace G_{0_k} and $\sigma^2_{0_k}$ with

786 G_k and σ^2_k, respectively. The error is given by the following equation:

787 $$\sigma_{r^2} \approx \frac{\sqrt{\sum_k \{2G_k G^*_k \sigma^2_k + (G^2_k + G^{*2}_k)(\alpha^2_k - \beta^2_k) + \eta^2_k\}}}{\sum_k G_{k0} G^*_{k0}} \quad (A11)$$

788

Figures

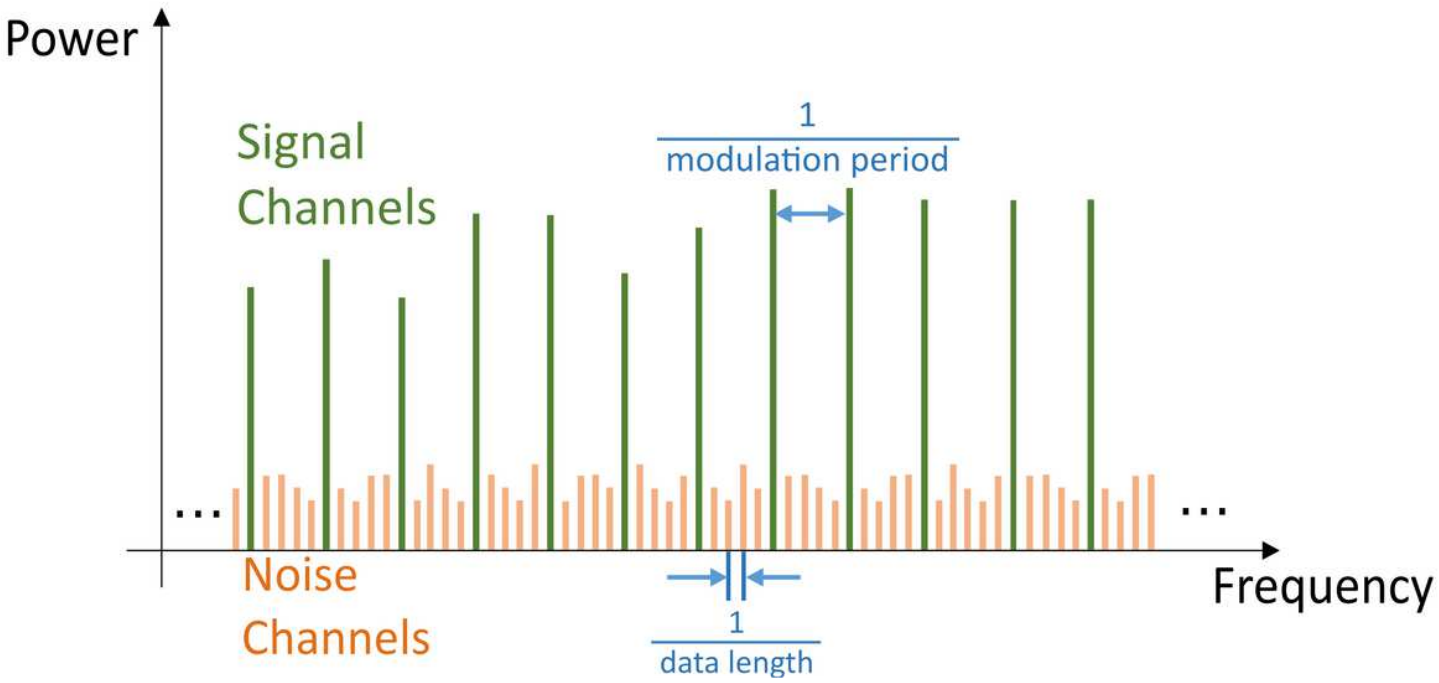

Figure 1

Characteristics of the ACROSS signal in frequency domain Typical distributions of the signal channels and noise channels in the frequency domain are illustrated. The signal channels appear at a constant interval, and noise channels appear in between. The intervals for the signal and noise channels are reciprocal of the modulation period and the data length, respectively.

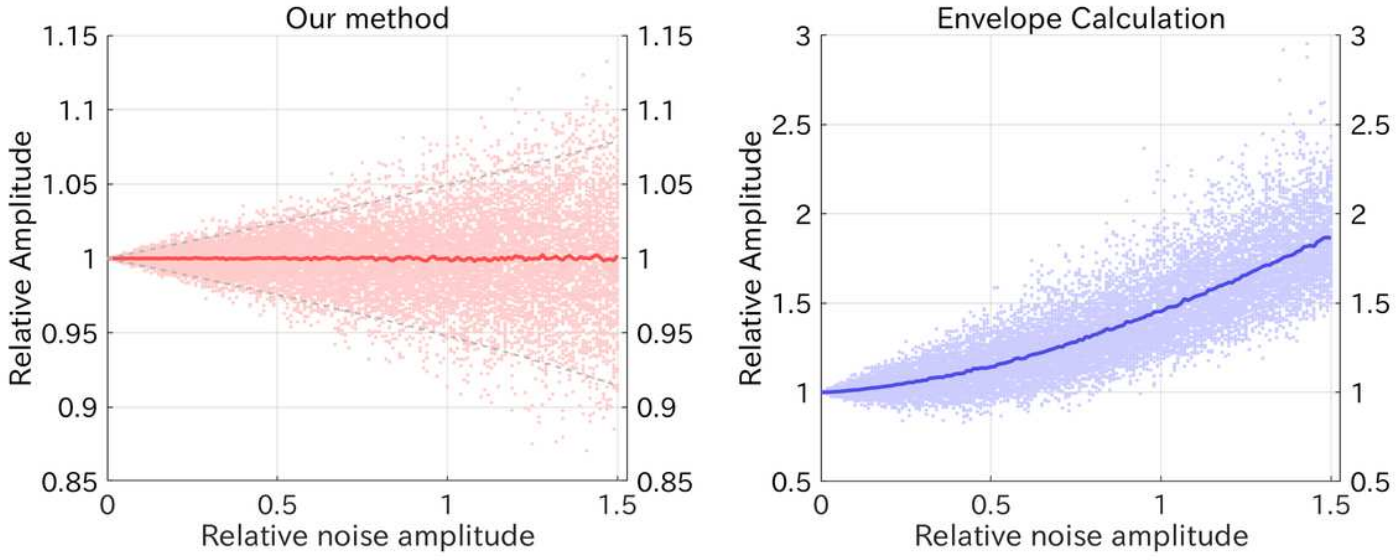

Figure 2

Result of the performance test Amplitudes estimated using our method and the envelope calculation are shown by the dots in the left and right panels, respectively. Horizontal axes indicate the amplitude of

noise relative to the root mean square of the signal. Vertical axes indicate the amplitude estimated with each method. The bold line shows the average of the calculation for each noise amplitude. The gray dashed line in the left panel indicates 95% confidence intervals, which are theoretically estimated from the noise amplitude.

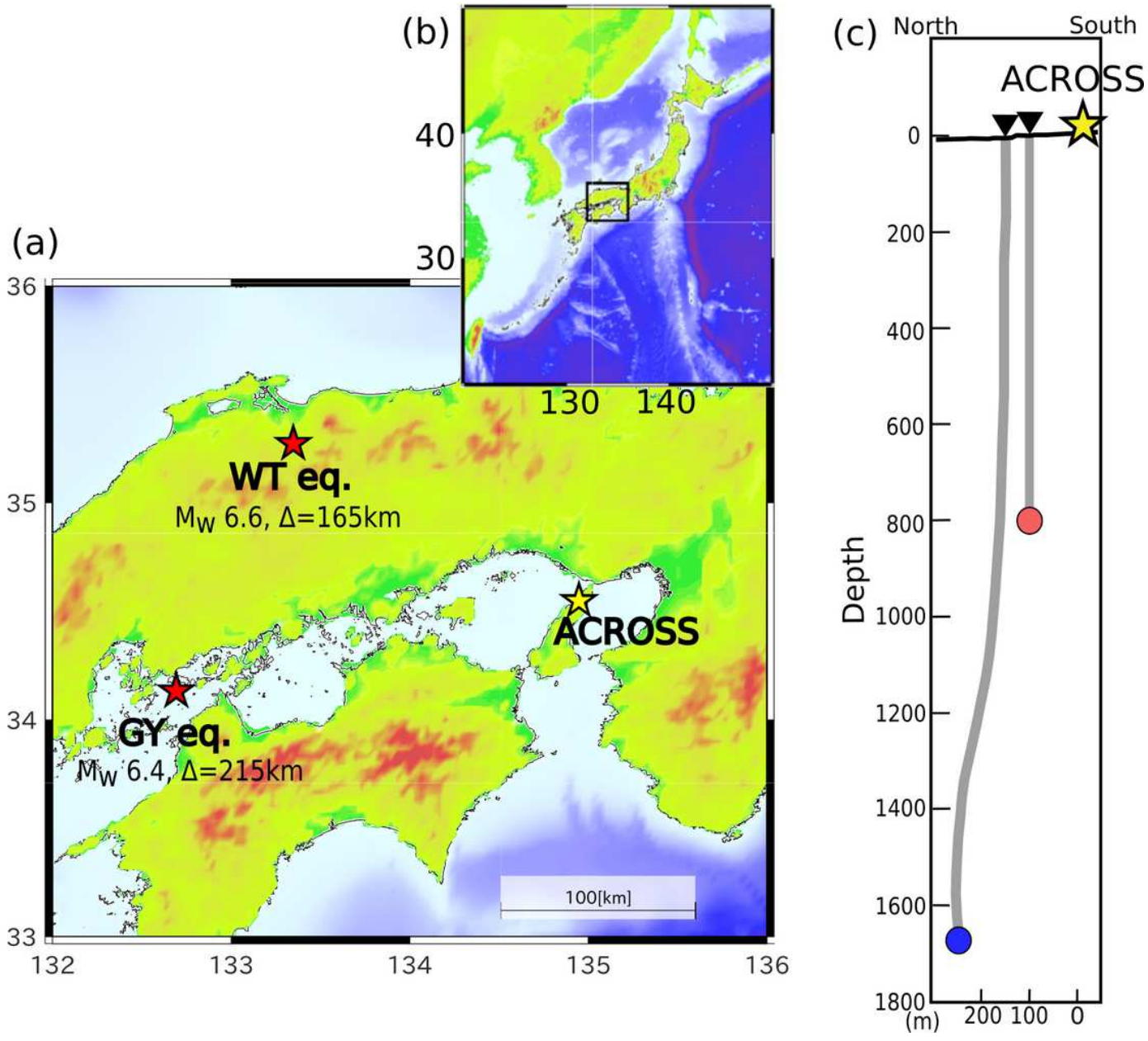

Figure 3

Location of ACROSS vibrators and borehole seismometers (a) Location of the site where ACROSS was deployed (yellow star) and epicenter of two earthquakes, which are mentioned in the text (red stars). The area of the map (a) is indicated by a black square in map (b). (c) Location of the ACROSS vibrator and borehole seismometers on a vertical cross section. The yellow star indicates the ACROSS vibrator. The red and blue circles show the 800 m and 1700 m sensors, respectively. Note: The designations employed and the presentation of the material on this map do not imply the expression of any opinion whatsoever on the part of Research Square concerning the legal status of any country, territory, city or area or of its

authorities, or concerning the delimitation of its frontiers or boundaries. This map has been provided by the authors.

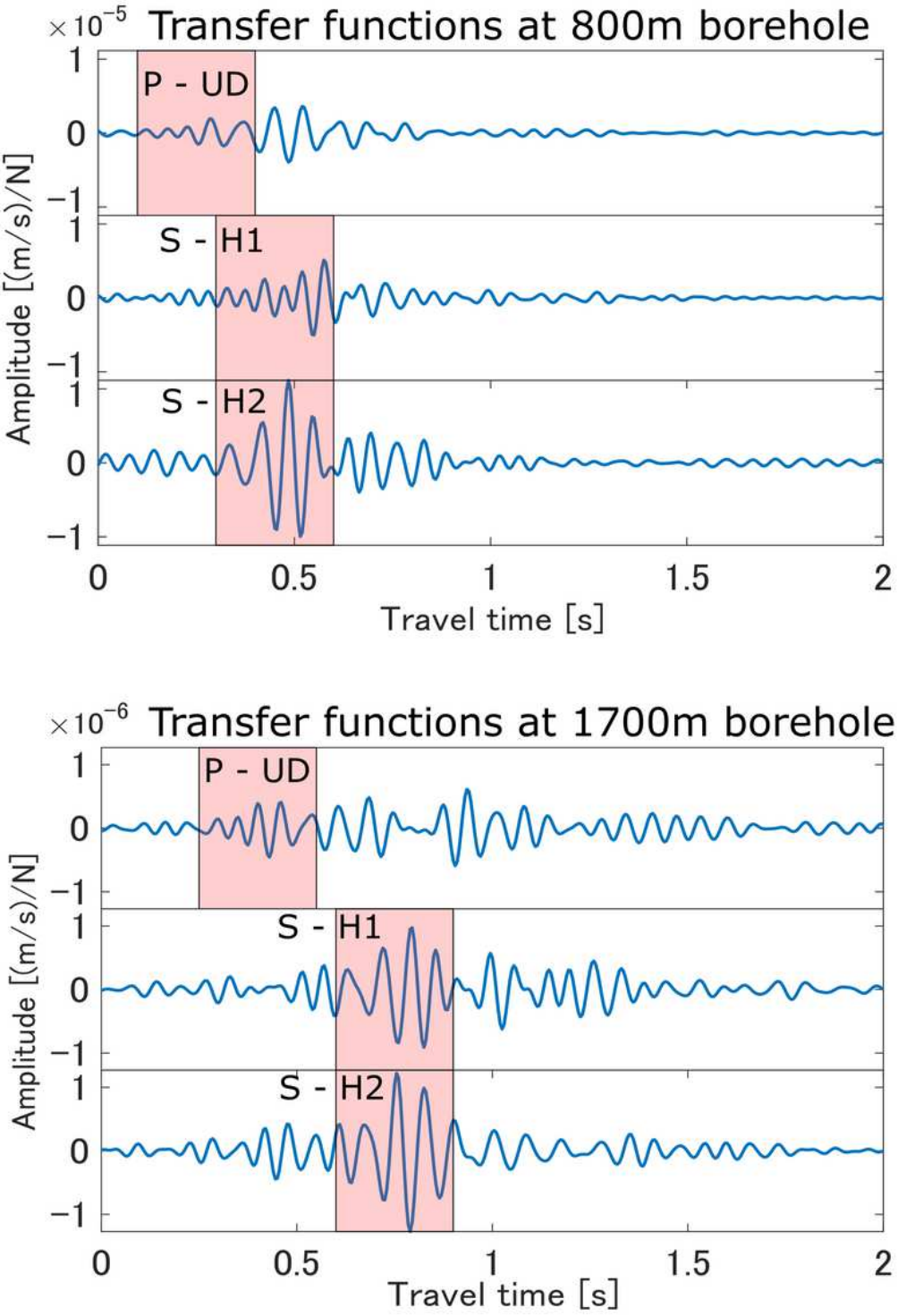

Figure 4

Reference transfer function in the time domain and selected P and S phases for the 800 m and 1700 m sensors. Transfer functions on 14:00 January 19, 2000, are used as references. The area with the red area

shows the P and S phases selected for calculating the change in amplitude and travel time. We selected P waves from the UD components (P-UD) and S waves from two horizontal components (S-H1 and S-H2).

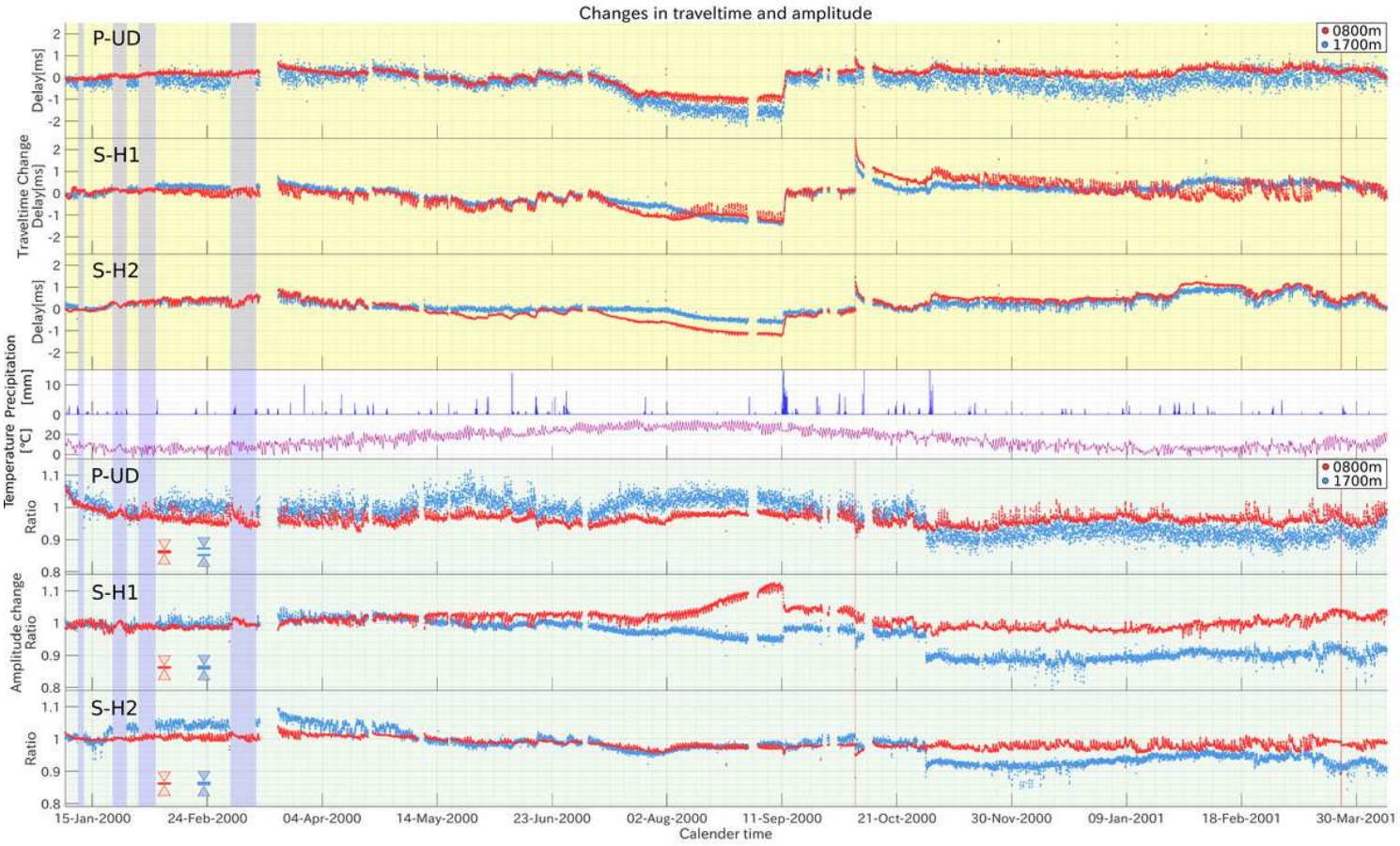

Figure 5

Change in travel time and amplitude throughout the observation period. The changes in travel time (top three panels with yellow background) are calculated according to Ikuta et al. (2002) and changes in amplitude (bottom three panels with green background) are obtained by our method. The two panels in the middle illustrate atmospheric temperature and rainfall observed at Gunka station, which is the nearest meteorological station of the Japan Meteorological Agency. Blue shading shows the periods of the water injection experiments. The red vertical lines show the time of the earthquakes mentioned in the text. The gap between horizontal lines with a pair of triangles in the left shows the mean error of the amplitude change calculated by Equation (6). The colors of the lines and triangles correspond to sensors in the legend on the right.

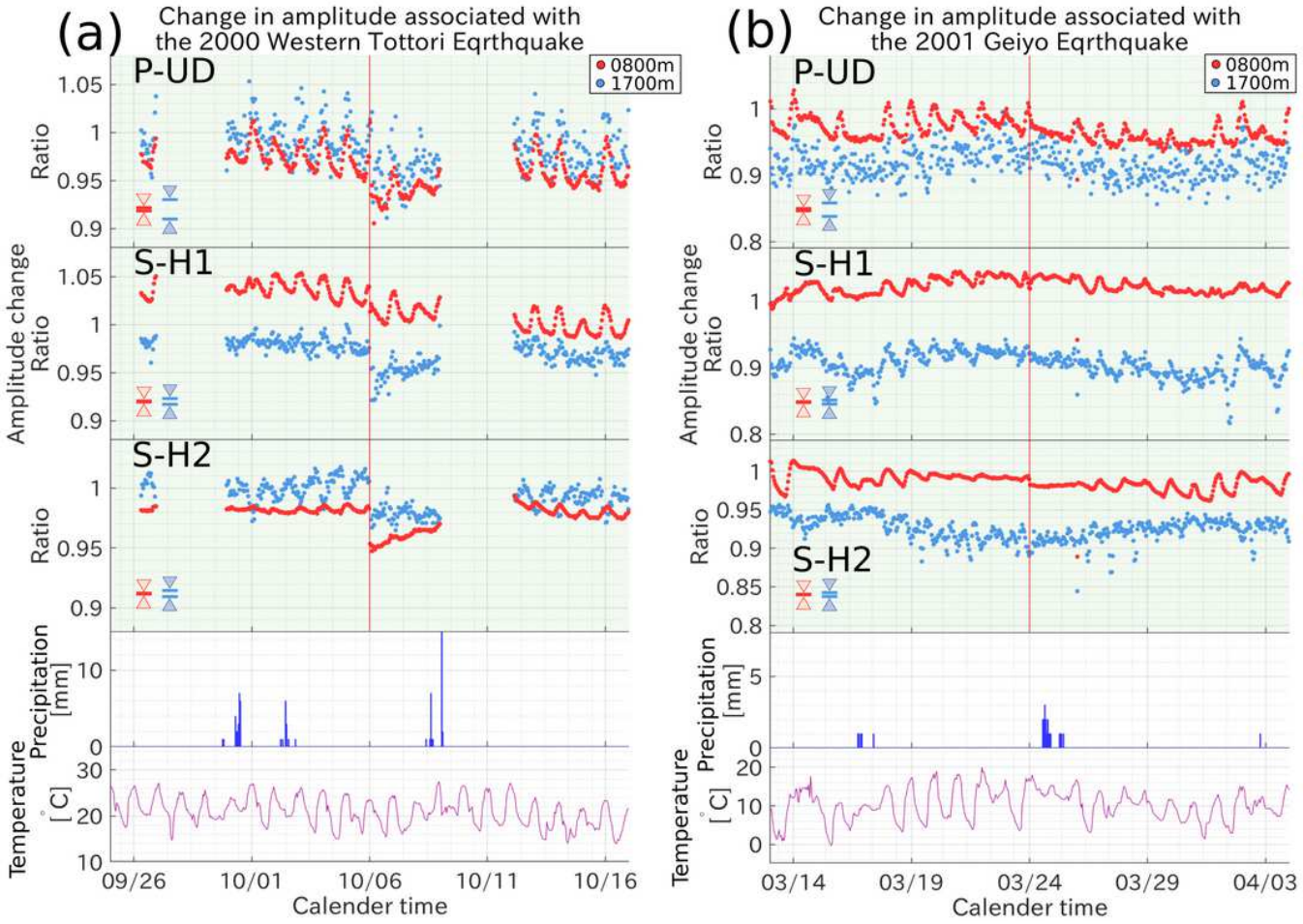

Figure 6

Changes in amplitudes 10 days before and after the 2000 Western Tottori (WT) and 2001 Geiyo (GY) earthquakes. The bottom row shows the temperature and rainfall at Gunka station. The gap between horizontal lines with a pair of triangles on the left of the panels shows the average error of the amplitude change.

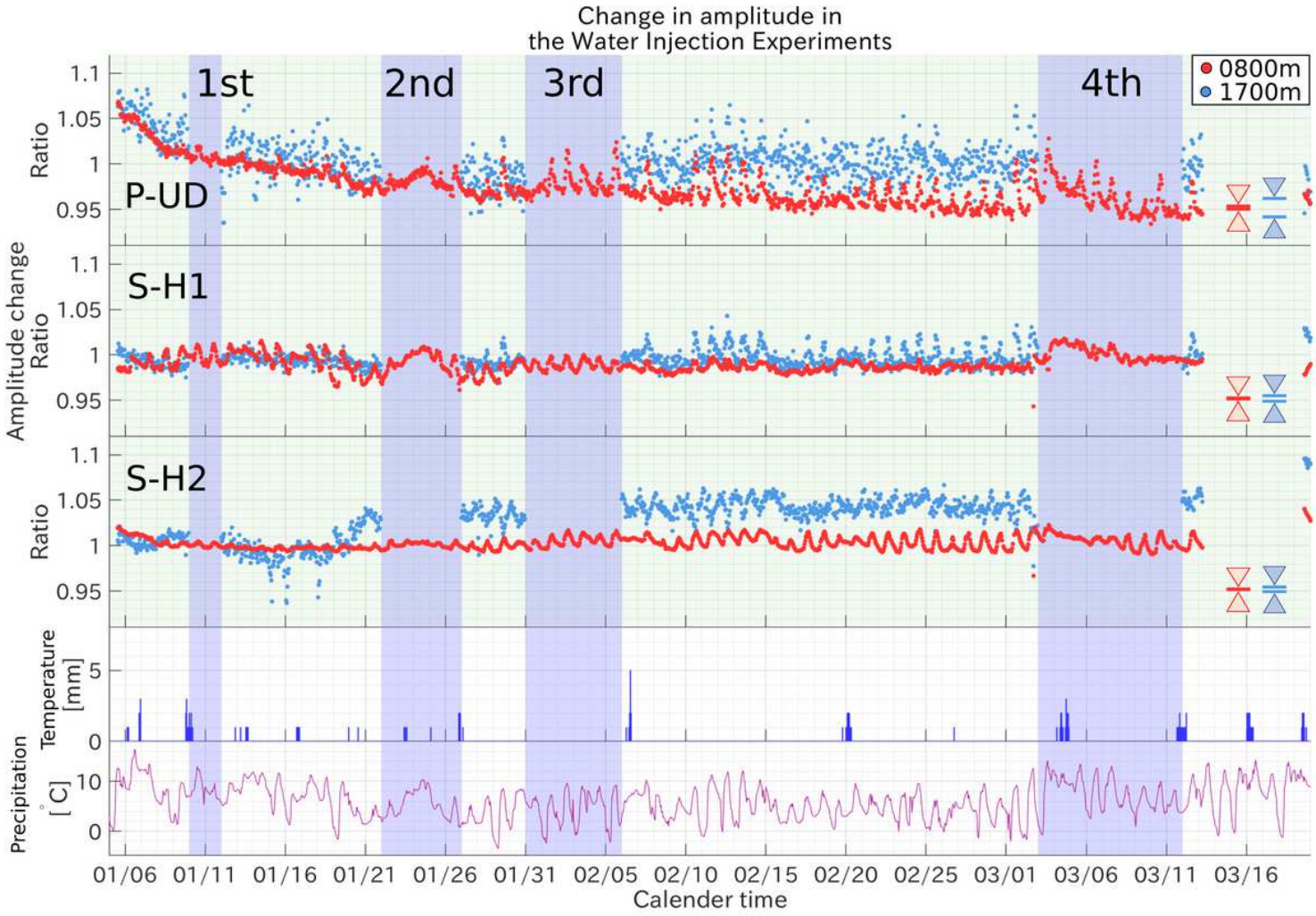

Figure 7

Change in amplitude during the period around the water injection experiments. The bottom row shows the temperature observed at the Gunka station. The blue background indicates the periods of the injection experiments. During the water injection experiment, the transfer function of the 1700 m sensor could not be analyzed because of the noise caused by the injection. The gap between horizontal lines with a pair of triangles on the right side of the panels show the mean error of the amplitude change.

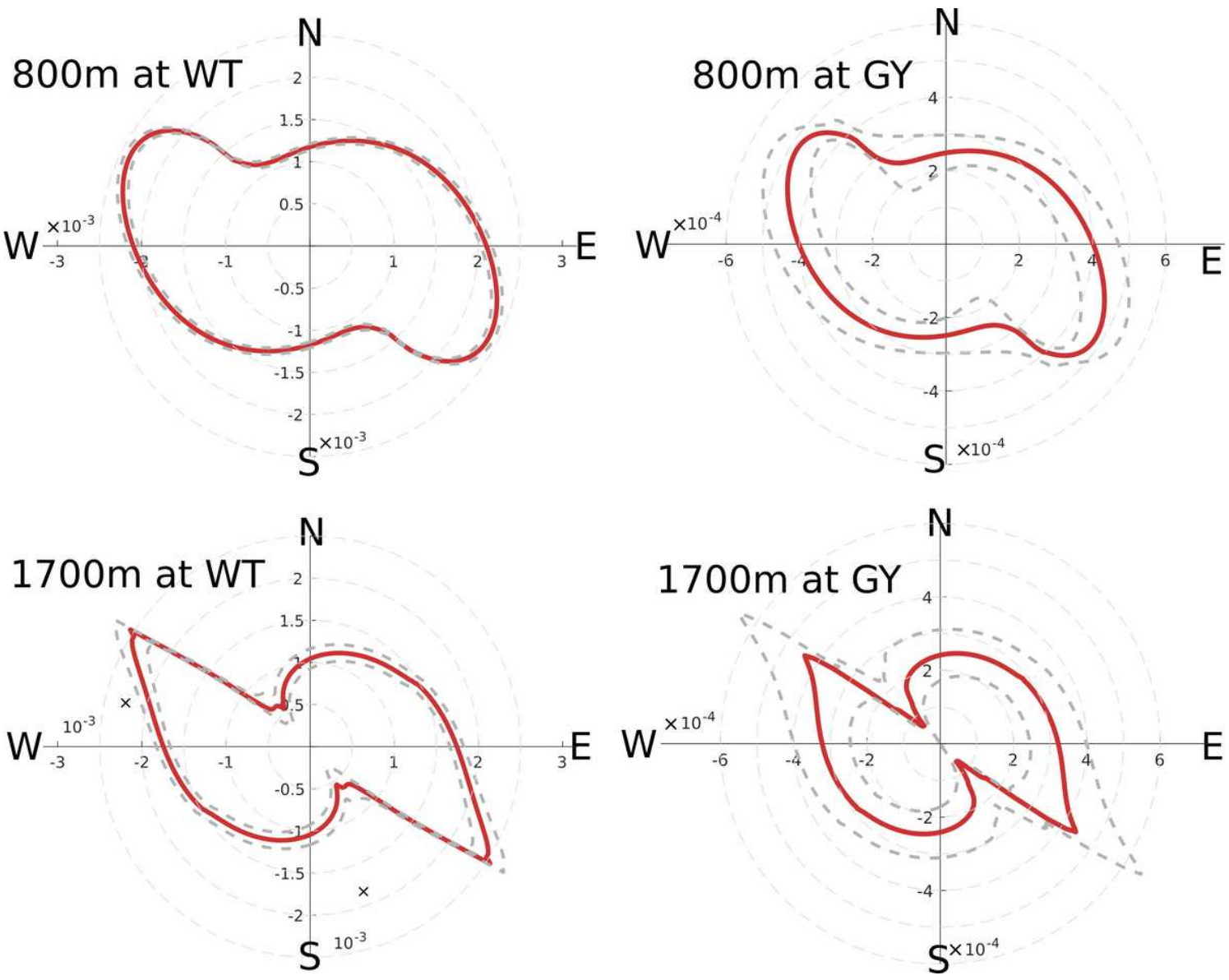

Figure 8

Azimuthal variation in the coseismic delay in travel time The red line shows the azimuthal variation in the coseismic delay. The vertical and horizontal axes indicate the NS and EW directions, respectively. Distances from the origin indicate coseismic delay. Gray dashed lines indicate 95% confidence intervals. The top and bottom panels show the results for the 800 m and 1700 m sensors. The left and right panels show the results for the WT and GY earthquakes, respectively.

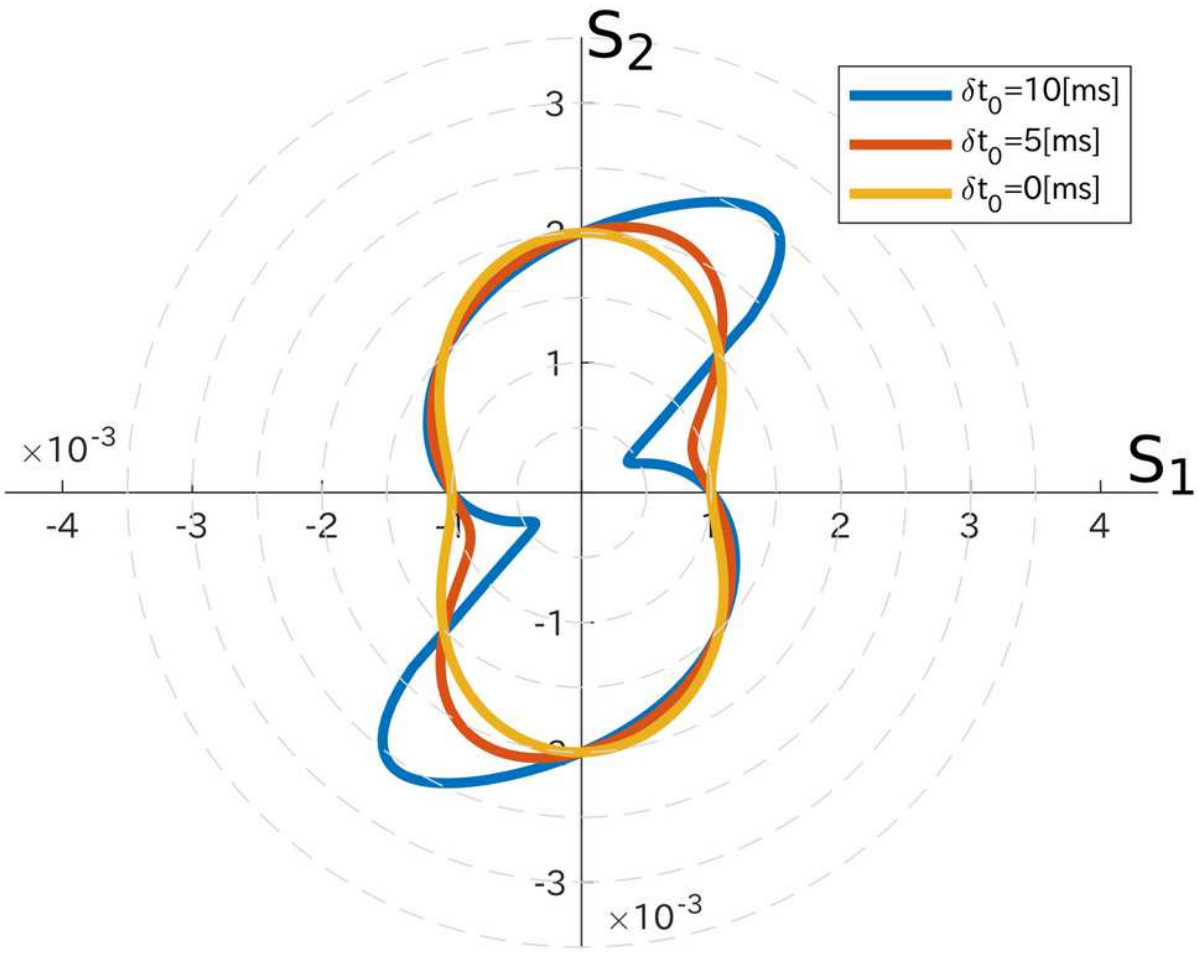

Figure 9

Examples of the synthetic azimuthal pattern Azimuthal variations of delays calculated by synthetic dataset are shown as examples. We showed three examples with 10, 5, and 0 ms of δt_0 in Equation (8). We provide A=1,δt_1=1 [ms],δt_2=2 [ms] in Equations (8) and (9) for this calculation.

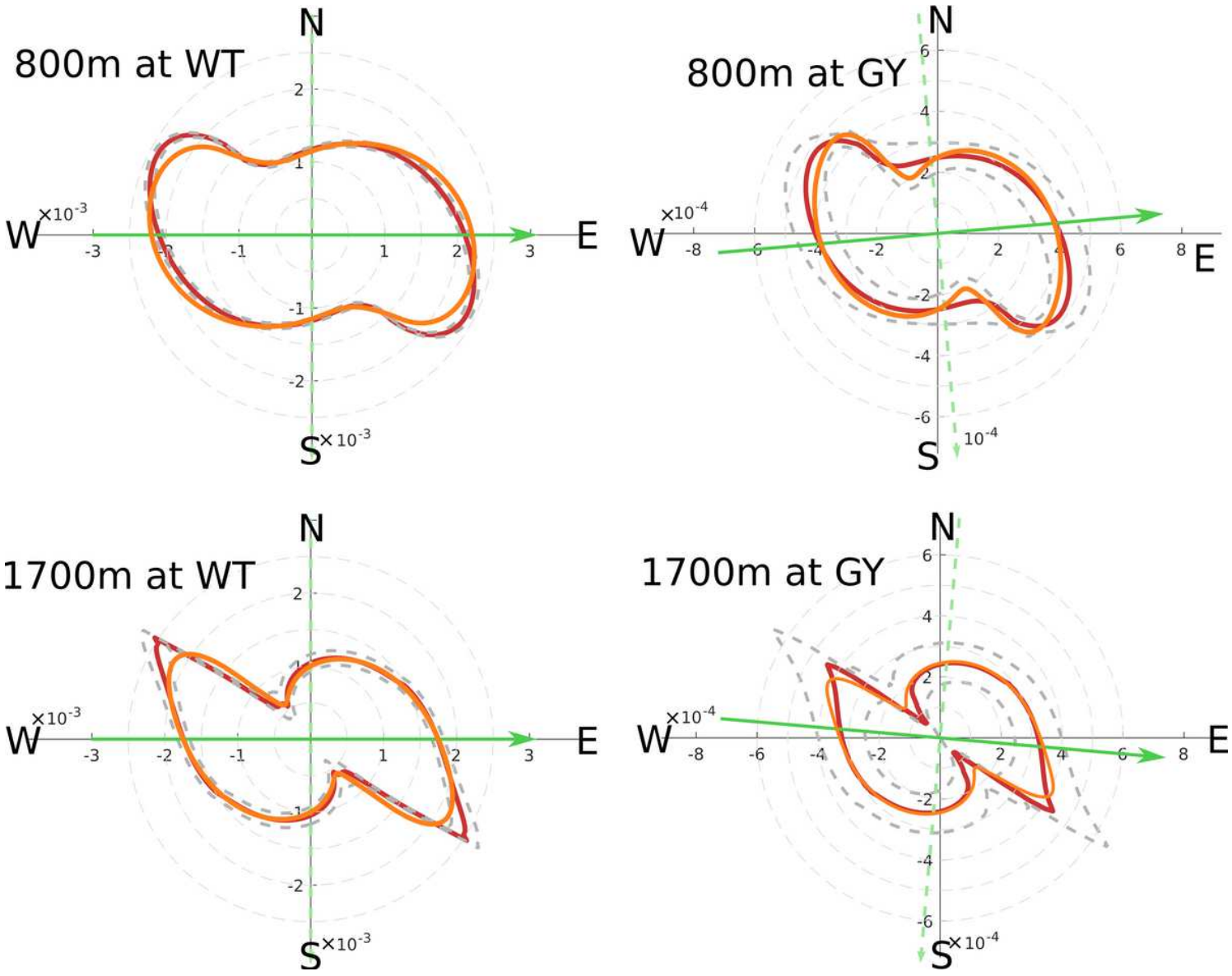

Figure 10

Principal axes of the coseismic delay estimated with the parameter estimation The red line shows the observed pattern. The orange line shows the synthetic pattern with the best parameter. Solid and dashed green lines show the major and minor axes of the principal axes, respectively. The top and bottom panels show the results for the 800 m and 1700 m sensors. The left and right panels show the results for the WT and GY earthquakes, respectively.

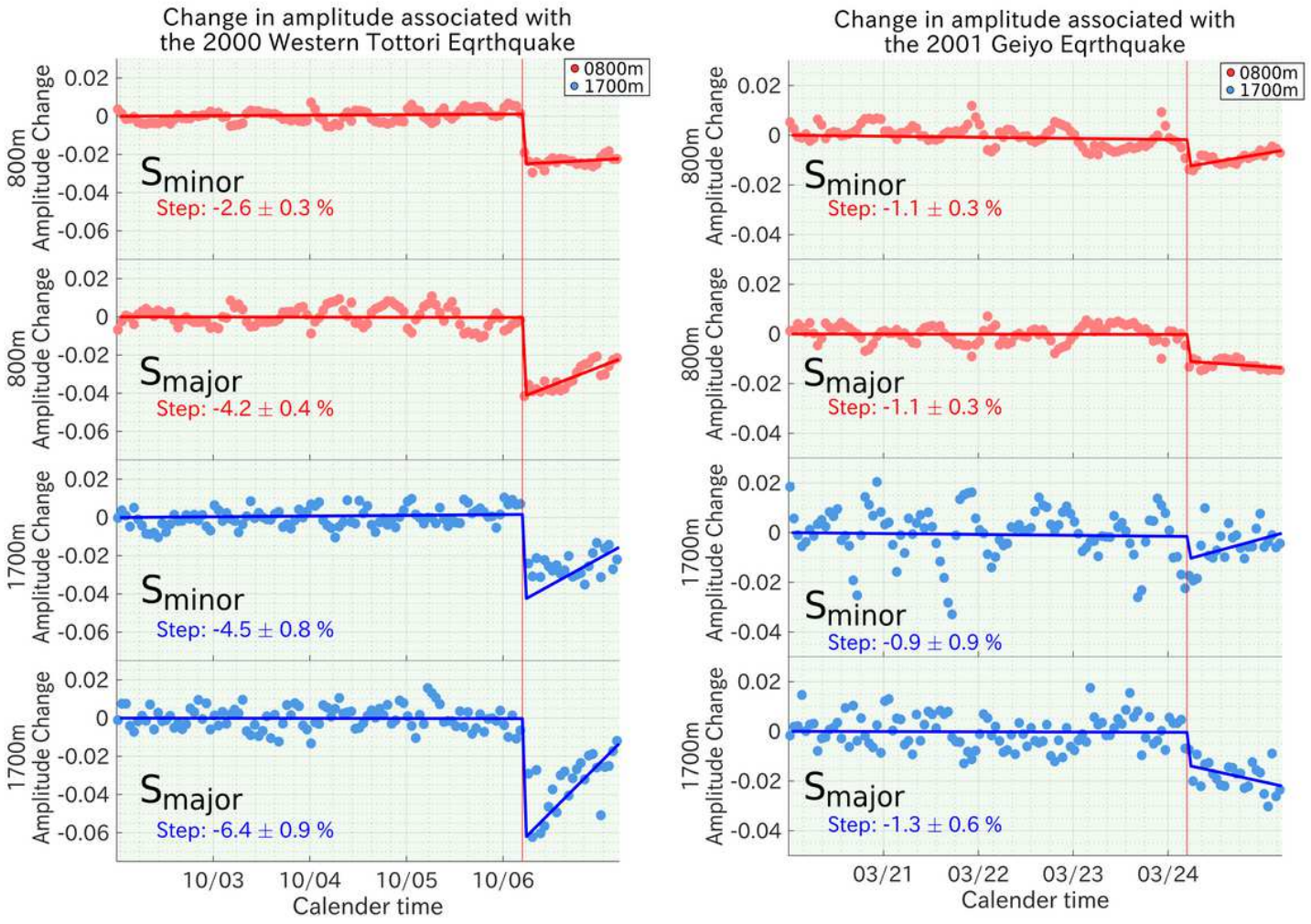

Figure 11

Coseismic decrease in amplitude in the principal axes of anisotropy Major and minor axes denote the direction of principal axes with larger and smaller delays in travel time, respectively. Variation in the amplitude (dots) and estimation with our model (solid line) in the principal axes are shown. The top two rows show the results for 800 m sensors and the bottom two rows show that for 1700 m sensors. The left and right panels show the results for the WT and GY earthquakes, respectively. The step and its estimation error are also shown on the left of each panel. The red vertical line shows the time of the earthquake.

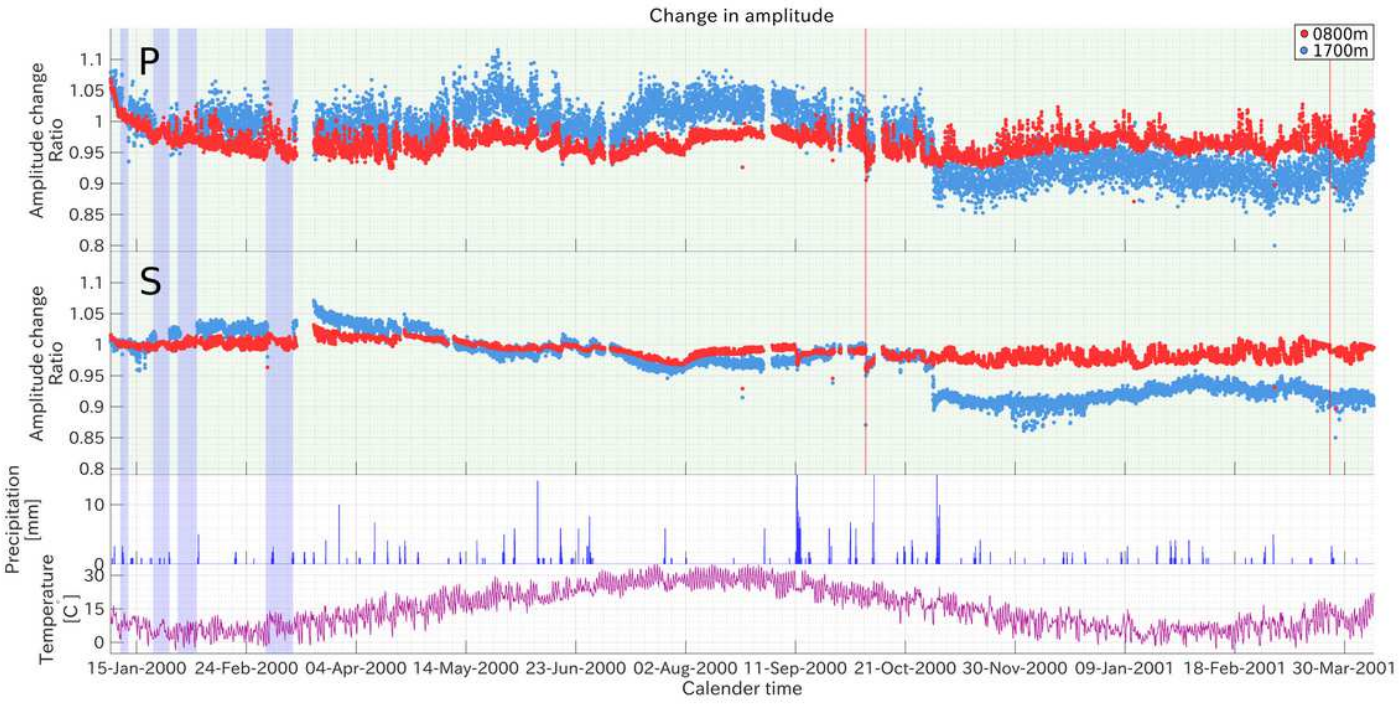

Figure 12

Changes in amplitude of the azimuthal invariant value. Changes in amplitude for P-UD and the azimuthal invariant value are shown in the top and second panels. The atmospheric temperature and rainfall are shown in the third and bottom panels. Periods with blue shading show the periods of the water injection experiments. The red vertical lines show the time of the WT and GY earthquakes.

Supplementary Files

This is a list of supplementary files associated with this preprint. Click to download.

- GraphicsAbstract.png